Nano Research

Open Access

Research Article

Engineering interfacial H-bond networks via orbital hybridization on $CuBiO_{2-x}$ to boost proton-coupled electron transfer for CO_2-to-HCOOH electrosynthesis

Jun Li[1] ✉, Peiyang Li[1], Shixuan Ge[1], Zhongyi Liu[1], Yangyang Zhang[1] ✉, and Bin Liu[2]

[1] *Henan Institute of Advanced Technology, College of Chemistry, State Key Laboratory of Coking Coal Resources Green Exploitation, Zhengzhou University, Zhengzhou 450001, China*
[2] *Department of Materials Science and Engineering, City University of Hong Kong, Hong Kong 999077, China*

Cite this article: *Nano Research*, **2026**, *19*, 94908687. https://doi.org/10.26599/NR.2026.94908687

ABSTRACT: The electrochemical CO_2 reduction reaction (CO_2RR) to formic acid (HCOOH) is constrained by slow kinetics and limited selectivity due to inefficient proton-coupled electron transfer (PCET). Herein, we synthesized Cu-doped BiO_{2-x} (CuBiO) nanosheets to facilitate proton transfer through reconstruction of the hydrogen-bond (HB) network, thereby accelerating the PCET process. The *in-situ* measurements reveal that part of the 4-coordinated hydrogen-bonded water (4-HB·H_2O) transforms into 2-coordinated hydrogen-bonded water (2-HB·H_2O) over CuBiO during CO_2RR. This reconstruction forms a linear proton transport pathway which efficiently promotes proton transport during PCET steps and concurrently inhibits the competing hydrogen evolution reaction. Density functional theory (DFT) calculations further elucidate that the Cu doping not only facilitates water dissociation into protons while inhibiting proton dimerization, but also enhances CO_2 activation and reduces the energy barrier for of $*CO_2 \rightarrow *OCHO$. Ultimately, the CuBiO-6 displays highly efficient conversion of CO_2 to HCOOH with a Faradaic efficiency (FE) of 92.4% and maintains stable operation for over 22 h. These findings provide a novel strategy to accelerate the PCET through regulation of interfacial HB network towards efficient CO_2RR to HCOOH.

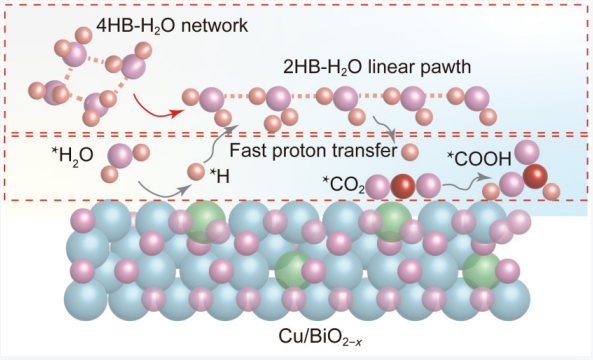

KEYWORDS: electrocatalytic CO_2 reduction, hydrogen-bond (HB) network, proton-coupled electron transfer, orbital hybridization, BiO_{2-x}, HCOOH

1 Introduction

The electrocatalytic carbon dioxide reduction reaction (CO_2RR), driven by renewable electricity, provides a promising pathway to achieving carbon neutrality [1–4]. Among various CO_2RR products, formic acid (HCOOH) represents one of the most economically viable liquid fuels [5–8]. The proton-coupled electron transfer (PCET) steps during the conversion of CO_2 to HCOOH are governed by the CO_2 activation and the interfacial water dissociation [9, 10]. Notably, interfacial water not only serves as a reactant providing proton but also assists proton transfer through the hydrogen-bond (HB) network [11–14]. This network primarily comprises two distinct water configurations: 4-coordinated hydrogen-bonded water (4-HB·H_2O) and 2-coordinated hydrogen-bonded water (2-HB·H_2O) [10]. In 4-HB·H_2O, each water molecule forms hydrogen bonds with four others, constructing a tightly interconnected three-dimensional network that may restricts proton transfer. In contrast, 2-HB·H_2O molecules are linked linearly through two hydrogen bonds, creating a favorable linear pathway for rapid proton transport. Therefore, the rational engineering of HB network within the interfacial water is crucial to accelerate PCET kinetics and thereby enhance the overall efficiency of CO_2RR.

Recently, significant advances have been made in promoting CO_2 to HCOOH using various transition metal electrocatalysts, including Pd, Bi, In, Sn [15–18], and their oxides (ZnO_x, BiO_x, InO_x, and CuO_x) [19–22]. Among these, Bi-based catalysts are particularly promising due to their low toxicity, economic viability,

Received: February 9, 2026; **Revised:** March 10, 2026
Accepted: March 30, 2026

✉Address correspondence to Yangyang Zhang, boniu87029286@zzu.edu.cn; Jun Li, junli2019@zzu.edu.cn

and suppressed hydrogen evolution reaction (HER) activity [23–25]. However, many Bi-based catalysts suffer from limited performance over wide and low-potential cathodic ranges, primarily owing to insufficient electrical conductivity and moderate selectivity toward HCOOH [26–28]. To overcome these challenges, various strategies such as defect engineering, alloying, doping, and nanostructuring have been actively explored to improve the catalytic properties of Bi-based systems [29–33]. Recently, many reports have demonstrated that the incorporation of d-block metals into Bi-based materials can lead to the formation of hybridized orbitals, greatly enhancing charge transport and optimizing the adsorption of key reaction intermediates to promote the CO_2RR activity [34–36]. Therefore, metal doping constitutes an effective approach for enhancing the efficiency and selectivity of the CO_2RR.

Herein, Cu-doped BiO_{2-x} (CuBiO) nanostructures were synthesized via a hydrothermal method. The prepared CuBiO-6 displayed excellent performance for CO_2RR to produce HCOOH with a Faradaic efficiency (FE) of 92.4%. *In-situ* measurements demonstrate that the Cu doping is in favour of strengthening the adsorption of $*CO_2^{\cdot-}$ and facilitates the construction of HB network of interfacial water, resulting in the fast proton transport pathway for HCOOH formation. The density functional theory (DFT) calculations show the accelerated water dissociation and inhibited HER over CuBiO, which promote sufficient proton for PCET. Besides, the Cu doping enhances the interaction between Bi sites and O atoms in $*CO_2$, facilitating the adsorption, activation and hydrogenation of CO_2. This study establishes a design principle for constructing multi-step electrocatalysts through the targeted introduction of cooperative active sites.

2 Materials and methods

2.1 Materials

The NaOH (≥ 99%), $NaBiO_3$ (80%), and $Cu(NO_3)_2{\cdot}3H_2O$ (99.99%) were purchased from Alfa. Tert-butanol (99%), PTFE (60 wt.%), and $KHCO_3$ (96%) were purchased from Innochem. Carbon paper and nafion 117 membrane were purchased from Canrd Technology Co., Ltd. All electrolyte solutions were prepared using Milli-Q water.

2.2 Catalyst preparation

Synthesis of BiO_{2-x} and Cu-doped BiO_{2-x}: BiO_{2-x} was synthesized via hydrothermal process. Specifically, 3.6 g of NaOH and 2.8 g of $NaBiO_3$ were dissolved in sequence in 60 mL of deionized water while being stirred. After 0.5 h, the suspension was placed in a 100 mL Teflon-lined stainless-steel container and subjected to heating at 180 °C for 6 h. After the system cooled to room temperature, the formed precipitate was separated by filtration, rigorously rinsed with deionized water and ethanol, and subsequently oven-dried at 60 °C for 12 h. Cu-doped BiO_{2-x} samples were prepared following the same procedure, except that different amounts of $Cu(NO_3)_2{\cdot}3H_2O$ were introduced to achieve Cu/Bi molar ratios of 2:100, 4:100, 6:100, and 8:100. The corresponding products were denoted as CuBiO-2, CuBiO-4, CuBiO-6, and CuBiO-8, respectively.

2.3 Characterization

Crystal structure was determined by X-ray diffraction (XRD) using a Bruker D8 diffractometer. Morphological characterization was performed by scanning electron microscope (Zeiss Sigma-360) and transmission electron microscope (JEOL JEM F200). Surface elemental composition and chemical states were analyzed via X-ray photoelectron spectroscopy (XPS) on a Thermo Fisher ESCALAB 250Xi. *In-situ* Fourier transform infrared (FTIR) spectra were collected with a Thermo Scientific Nicolet iS50 spectrometer equipped with a liquid-nitrogen-cooled MCT detector.

2.4 Preparation of working electrode

To make a homogeneous catalyst ink, 5 mg of catalyst powder was mixed into 960 μL of ethanol and 40 μL of PTFE solution (0.1 wt.%), and then sonicated for 1 h. Then, 1 mL of the ink was uniformly layered onto a piece of hydrophilic carbon paper of 1 cm × 1 cm, achieving a catalyst loading of 5 mg/cm^2.

2.5 Electrocatalytic measurements

All electrochemical measurements were performed in a standard three-electrode H-cell (15 mL), partitioned by a Nafion 117 membrane, using a CHI660E potentiostat at ambient temperature. The cell contained a CO_2-saturated 0.1 M $KHCO_3$ electrolyte (15 mL), with a saturated Ag/AgCl electrode and a carbon rod serving as the reference and counter electrode, respectively. Chronoamperometry was conducted sequentially from −1.0 to −1.4 V (vs. reversible hydrogen electrode (RHE)).

2.6 Product quantification

The gas chromatograph (SHIMADZU 2014) with thermal conductivity detector (TCD) and flame ionization detector (FID) detectors was employed to monitor the gas-phase products (H_2 and CO). For measuring liquid products like HCOOH, 1H-nuclear magnetic resonance (NMR) spectra were recorded using a 400 MHz Bruker spectrometer. The electrolyte (200 μL) after tests was mixed with 100 μL of 10 mM dimethyl sulfoxide (DMSO) as an internal standard and diluted with 100 μL of D_2O. The peak areas of HCOOH were measured relative to the internal DMSO peak area.

(1) The FE of HCOOH, CO, or H_2 was determined via Eq. (1)

$$\mathrm{FE} = \frac{Q}{Q_{\mathrm{total}}} = \frac{n \times N \times F}{Q_{\mathrm{total}}} \tag{1}$$

where Q is the charge used for reducing the product (HCOOH, CO, or H_2) (C), Q_{total} is the total charge (C), n is the number of electrons transferred for product formation, N is the number of moles of CO or H_2 (mol), and F is the Faradaic constant (96,485 C/mol).

(2) The yield rate of HCOOH was determined using Eq. (2)

$$\text{Yield rate} = \frac{N}{tS} \tag{2}$$

where N is the number of moles for HCOOH (mol), t is the electrolysis time (h), and S is the catalyst surface area (cm^2).

2.7 DFT calculations

The DFT computations were conducted within the Vienna *ab initio* simulation package (VASP) framework [37]. Electron–core interactions and exchange-correlation effects were described using the projector augmented wave (PAW) method [38] and the Perdew–Burke–Ernzerhof generalized gradient approximation (PBE-GGA) functional [39], respectively. A cutoff energy of 500 eV was set for the plane-wave basis. Geometry relaxations utilized the

conjugate gradient algorithm, with convergence criteria of 10^{-5} eV in energy and 0.02 eV/Å in force. Integration over the Brillouin zone employed a Γ-centered 3 × 3 × 1 *k*-point mesh, supplemented by the DFT-D3 scheme for dispersion corrections [40]. Finally, the Gibbs free energy at 298.15 K was calculated for all relevant species (gaseous and adsorbed) according to Eqs. (3)–(6)

$$G = E_{DFT} + E_{ZPE} - TS \quad (3)$$

$$E_{ZPE} = \sum_i \frac{1}{2}\hbar\nu \quad (4)$$

$$\Theta_i = \hbar\nu_i / k \quad (5)$$

$$S = \sum_i R[\ln(1 - e - \Theta_i/T) - 1 + \Theta_i T(e\Theta_i/T - 1) - 1)] \quad (6)$$

where E_{DFT} is the electronic energy of the optimized geometry, E_{ZPE} is the zero-point energy, S denotes the entropy, $\hbar$ is the Planck constant, ν is the computed frequencies of vibratio, Θ_i is the vibration temperature, k is the constant of Boltzmann, and R is the constant of molar gas.

For adsorbed species, all 3N vibrational degrees of freedom are regarded as frustrated harmonic modes.

Subsequently, the climbing-image nudged elastic band (CI-NEB) method was used to calculate the minimum energy pathways and associated transition states [41]. To quantitatively probe chemical bonding interactions, particularly those between the catalyst surface and critical intermediates, crystal orbital Hamilton population (COHP) analysis was conducted using the LOBSTER code [42].

3 Results and discussion

3.1 Materials characterization

The synthesis process of BiO_{2-x} and CuBiO nanosheets is illustrated in Fig. 1(a) [43]. The XRD patterns of BiO_{2-x} and CuBiO with different Cu/Bi ratios are shown in Fig. 1(b). The peaks at 28.2°, 32.7°, 46.5°, 55.6°, and 58.3° of BiO_{2-x} can be attributed to cubic BiO_{2-x} (PDF No. 47-1057) [43–45]. The CuBiO catalysts exhibit the same XRD patterns as BiO_{2-x}, with no diffraction peaks corresponding to metallic Cu or Cu oxides, indicating that the Cu atoms were successfully incorporated into BiO_{2-x}. The investigation

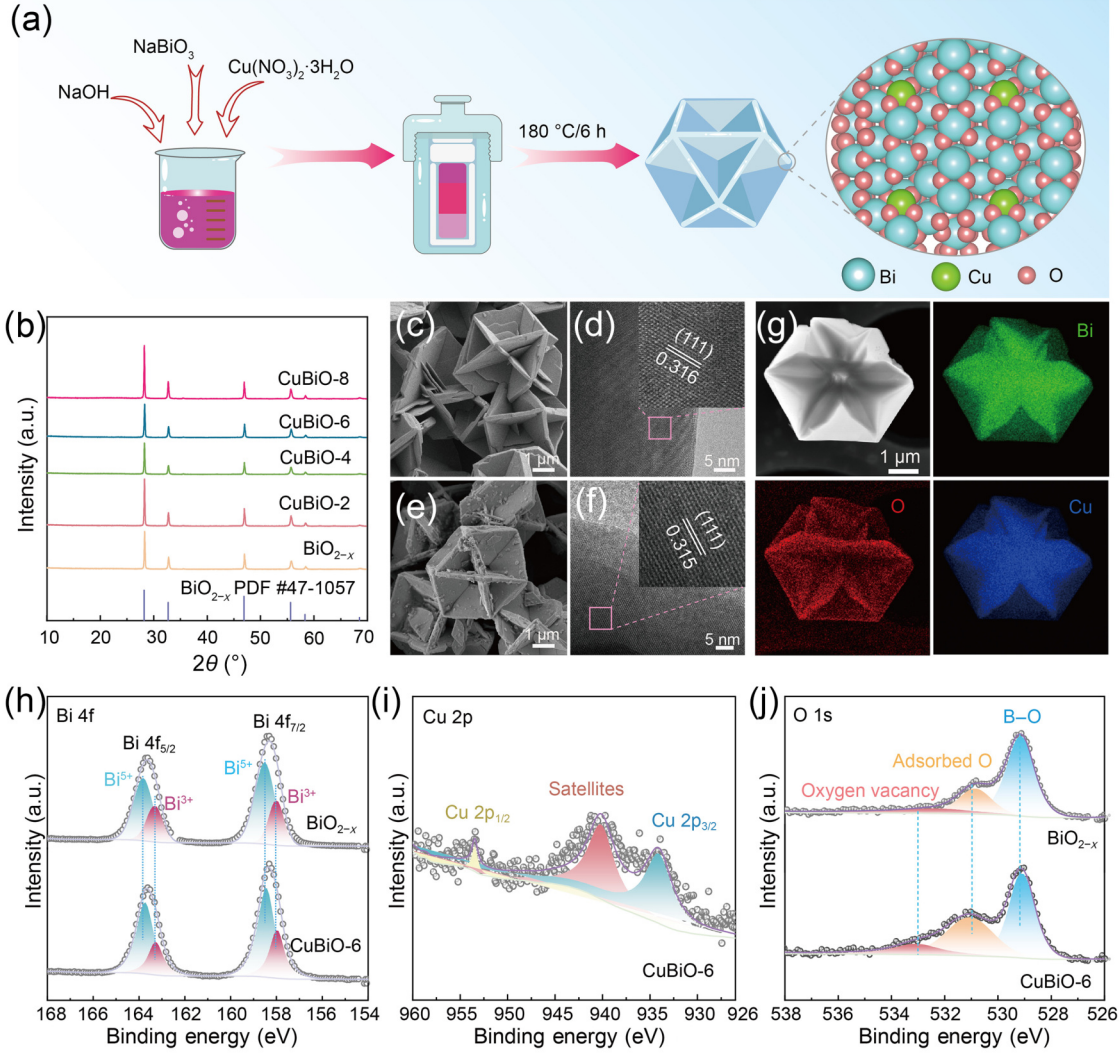

Figure 1 (a) Schematic illustration of the synthesis process of Cu-doped BiO_{2-x}. (b) XRD patterns of BiO_{2-x} and Cu-doped BiO_{2-x}. ((c) and (d)) SEM and HRTEM images of BiO_{2-x}. ((e) and (f)) SEM and HRTEM images of Cu-doped BiO_{2-x}. (g) TEM-EDX element mapping of Cu-doped BiO_{2-x}. ((h)–(j)) XPS spectra of (h) Bi 4f, (i) Cu 2p, and (j) O 1s of BiO_{2-x} and Cu-doped BiO_{2-x}.

of morphology and crystal structure was carried out using scanning electron microscopy (SEM) and transmission electron microscopy (TEM). The SEM images in Fig. 1(c) and Fig. S1(a) in the Electronic Supplementary Material (ESM) reveal that BiO_{2-x} exhibits smooth hexagonal nanosheets intersecting with each other. The high-resolution TEM (HRTEM) image of BiO_{2-x} shows a lattice fringe distance of 0.316 nm corresponding to the (111) plane of cubic BiO_{2-x} (Fig. 1(d)) [46]. The CuBiO catalysts exhibit a morphology similar to that of BiO_{2-x} but possess a rougher surface, which provides additional active area (Fig. 1(e) and Fig. S1(b) in the ESM). The CuBiO lattice spacing of 0.315 nm (Fig. 1(f)) is consistent with BiO_{2-x}, indicating that Cu incorporation does not alter the crystalline structure. The TEM energy-dispersive X-ray (EDX) spectroscopy mappings display the uniform distribution of elements within the BiO_{2-x} (Fig. S2 in the ESM) and CuBiO (Fig. 1(g)). XPS was carried out to elucidate the chemical states of elements in the synthesized catalysts. The XPS peaks of BiO_{2-x} located at 158.55 and 163.84, and 158.02 and 163.34 eV are attributed to Bi^{5+} and Bi^{3+}, respectively (Fig. 1(h)) [45, 47]. The binding energy of Bi in CuBiO shifts toward the positive direction (158.47 and 163.73, and 157.97 and 163.25 eV) compared with BiO_{2-x}, indicating electron redistribution after Cu doping. The XPS spectrum of Cu 2p (Fig. 1(i)) shows peaks at 953.5 and 934.1 eV corresponding to Cu $2p_{1/2}$ and Cu $2p_{3/2}$ of Cu^{2+}, respectively [48–50]. The XPS spectrum of O 1s can be deconvoluted into three peaks at 529.2, 530.9, and 532.6 eV, attributed to lattice oxygen, chemically adsorbed oxygen, and oxygen vacancy, respectively [44, 45]. These results confirm that Cu^{2+} was successfully doped into BiO_{2-x}, which may induce distinct electrochemical properties.

3.2 Electrochemical performances of CO_2RR

The electrochemical performance of BiO_{2-x} and CuBiO was evaluated in a standard three-electrode H-cell. The activity of HER was first examined in 0.1 M $KHCO_3$ (Fig. S3 in the ESM). Compared with pure BiO_{2-x}, the current density increases after Cu doping, indicating that the introduction of Cu facilitates HER. Figure 2(a) shows the linear sweep voltammetry (LSV) curves of CO_2RR in 0.1 M $KHCO_3$ electrolyte saturated with CO_2. BiO_{2-x}

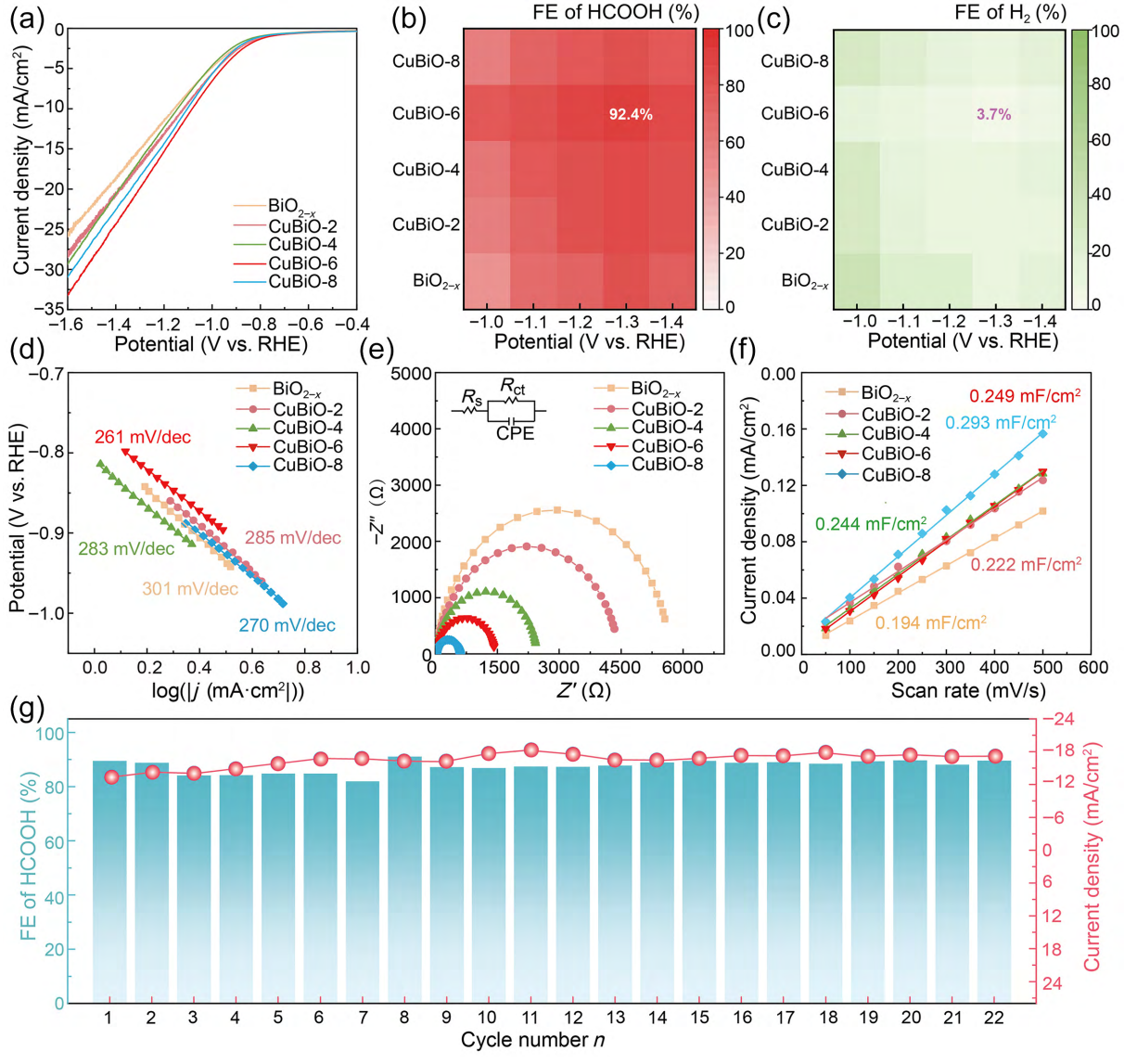

Figure 2 (a) LSV curves of BiO_{2-x} and CuBiO. ((b) and (c)) The FE of HCOOH and H_2, respectively. (d) Tafel slopes, (e) EIS, and (f) ECSA curves of BiO_{2-x} and CuBiO. (g) Stability test.

exhibits poor CO_2RR activity, as indicated by the lowest current density. After Cu incorporation, the current density increases. Notably, CuBiO-6 displays the highest current density, demonstrating superior CO_2RR activity. The CO_2RR products after chronoamperometry tests (Figs. S4–S8 in the ESM) were detected by online gas chromatography (GC) and 1H NMR spectroscopy. The representative NMR data shown in Fig. S9 in the ESM confirm the formation of HCOOH during CO_2RR. As shown in Fig. 2(b) and Fig. S10 in the ESM, CuBiO-6 demonstrates remarkable selectivity toward the CO_2RR, achieving superior FE, yield rate, and partial current density for HCOOH production. In particular, a peak FE of 92.4% is attained at a potential of −1.3 V vs. RHE. The lowest FE of H_2 catalyzed by CuBiO-6 in Fig. 2(c) illustrates the inhibited HER. The FE for CO remains below 10% across the tested potentials (Fig. S11 in the ESM), indicating that CO_2 is predominantly converted to HCOOH. This excellent performance of CuBiO-6 indicates that incorporating Cu species plays a critical role to promote the catalyst's selectivity toward HCOOH formation. The kinetic behavior of the reaction was probed via Tafel plot analysis, as illustrated in Fig. 2(d). A diminished Tafel slope is indicative of accelerated reaction kinetics. The Tafel slopes of BiO_{2-x}, CuBiO-2, CuBiO-4, CuBiO-6, and CuBiO-8 are 301, 285, 283, 261, and 270 mV/dec, respectively. Notably, CuBiO-6 shows the smallest Tafel slope, indicating the enhanced kinetics. Electrochemical impedance spectroscopy (EIS) was used to reveal the resistance of the catalysts. As shown in Fig. 2(e), CuBiO exhibits a smaller charge-transfer resistance (R_{ct}) value compared with BiO_{2-x}, indicating that Cu doping significantly promotes electron-transfer kinetics due to the lower R_{ct}. In addition, the electrochemically active surface areas (ECSA) of the catalysts were estimated by evaluating the electrochemical double-layer capacitances (C_{dl}) under non-Faradaic conditions (Figs. S12–S16 in the ESM). The larger C_{dl} value of CuBiO indicates a larger ECSA (Fig. 2(f)), which greatly accelerates the CO_2RR process. The long-term electrochemical stability of CuBiO-6 was assessed via chronoamperometry at −1.3 V vs. RHE. As shown in Fig. 2(h), the catalyst retained a steady current density of approximately 17.4 mA/cm^2 over 22 h, while the FE for HCOOH remained consistently around 90%. The HRTEM image and XPS spectra of CuBiO-6 after tests revealed that the cubic BiO_{2-x} structure of CuBiO-6 was well preserved (Figs. S17 and S18 in the ESM), confirming its excellent structural and catalytic stability under CO_2RR conditions. Table S1 in the ESM summarizes the CO_2RR performance of CuBiO-6 against recently documented Bi-based and Cu-doped electrocatalysts. In terms of FE, potential, partial current density, and durability, CuBiO-6 manifests markedly superior catalytic performance.

3.3 Mechanisms of CO_2RR via *in-situ* spectra

The *in-situ* FTIR measurements were conducted to clarify the mechanism of CO_2RR. As shown in Fig. 3(a), the peaks located at 1222, 1347, and 2360 cm^{-1} over BiO_{2-x} originate from the vibrations of $*CO_2^{\bullet-}$, *HCOO, and $*CO_2$, respectively [51–53]. The $*CO_2^{\bullet-}$ species is the key intermediate during CO_2 electroreduction to HCOOH, while the *HCOO vibration corresponds to the product signal. With increasing cathodic potential, the $*CO_2^{\bullet-}$ vibration shifts negatively due to the Stark effect, accompanied by enhanced absorption intensity. CuBiO-6 displays stronger $*CO_2^{\bullet-}$ and *HCOO signals compared with BiO_{2-x} under the same conditions (Fig. 3(b)). The exact intensity and changes of the $*CO_2^{\bullet-}$ stretching wavenumber are shown in Fig. 3(c). CuBiO-6 shows larger intensity and a higher Stark tuning rate, indicating stronger $*CO_2^{\bullet-}$ adsorption relative to BiO_{2-x}. To elucidate the role of proton in the CO_2RR, we introduced tert-butanol (TBA) into the electrolyte as a proton quencher. As shown in Fig. S19 in the ESM, the addition of TBA led to a decrease in the HCOOH yield, suggesting that the availability of protons is crucial for HCOOH production. The proton in HCOOH originates from water dissociation. Therefore the influence of interfacial water on CO_2RR was studied through Gaussian fitting of the *in-situ* FTIR spectra. The O–H vibration peak can be divided into three peaks corresponding to 4-HB·H_2O, 2-HB·H_2O, and ion-hydrated water (ionized H_2O), respectively (Figs. 3(d) and 3(e), and Table S2 in the ESM) [54–56]. The distinct HB network of interfacial water critically influences proton transport and reaction pathways during CO_2 reduction. The 4-HB·H_2O forms a three-dimensional (3D) HB network that impedes efficient proton transfer between catalytic sites. The 2-HB·H_2O forms a two-dimensional (2D) structure that provides a favorable linear pathway for proton transport. As shown in Fig. 3(f), the initial areas of the H_2O peaks on CuBiO-6 are larger than those on BiO_{2-x}, indicating stronger H_2O adsorption on the CuBiO-6 surface. This enhanced adsorption promotes the hydrogenation process of CO_2RR. Notably, as the applied potential becomes more cathodic, the HB network of interfacial water structure undergoes a distinct evolution: The proportion of 4-HB·H_2O decreases, while the proportions of 2-HB·H_2O and ionized H_2O species increase (Fig. 3(g)). Notably, the CuBiO-6 shows the higher proportion of 2-HB·H_2O than that of BiO_{2-x}. The reconstructed HB network with more 2-HB·H_2O network offers a linear pathway for proton transport over CuBiO-6, significantly facilitating the PCET process during CO_2RR.

3.4 Mechanisms of CO_2RR via DFT calculation

DFT calculations were performed to gain further mechanistic insight. As illustrated in Fig. 4(a), the energy barrier for H_2O dissociation on CuBiO-6 (0.16 eV) is significantly lower than that on BiO_{2-x} (0.29 eV). Moreover, CuBiO-6 exhibits a higher energy barrier for *H dimerization to H_2 (1.42 vs. 1.04 eV on BiO_{2-x}; Fig. 4(b)), indicating that Cu doping promotes water dissociation while suppressing HER, thereby supplying more *H for CO_2 hydrogenation. As illustrated by the partial density of states (PDOS) in Fig. 4(c), the significant overlap of the Cu 3d and O 2p states near the Fermi level in CuBiO-6 indicates strong d–p orbital hybridization. To elucidate the electronic coupling mechanism, schematic representations of the hybrid Cu–O molecular orbitals and the corresponding energy level alignment are provided in Figs 4(d) and 4(e), respectively. The d–p hybridization facilitates electron transfer from Cu to O, leading to the presence of unpaired d-electrons near the Fermi level. This electronic configuration significantly strengthens the adsorption of reactants, thereby promoting catalytic performance. A quantitative assessment of Bader charge and adsorption energy (E_{ads}) was performed to elucidate CO_2 adsorption behavior on the catalyst surfaces (Figs. 4(f) and 4(g)). Relative to BiO_{2-x}, which exhibits an adsorption energy of –0.43 eV and a Bader charge transfer of 0.05 e, CuBiO-6 demonstrates a more negative $*CO_2$ adsorption energy (–0.52 eV) and an increased Bader charge transfer (0.13 e). This comparative analysis indicates the enhanced CO_2 adsorption affinity of CuBiO-6. COHP analysis was applied to assess the bonding between Bi sites and O atoms in $*CO_2$ (Figs. 4(h) and 4(i)). The integrated COHP

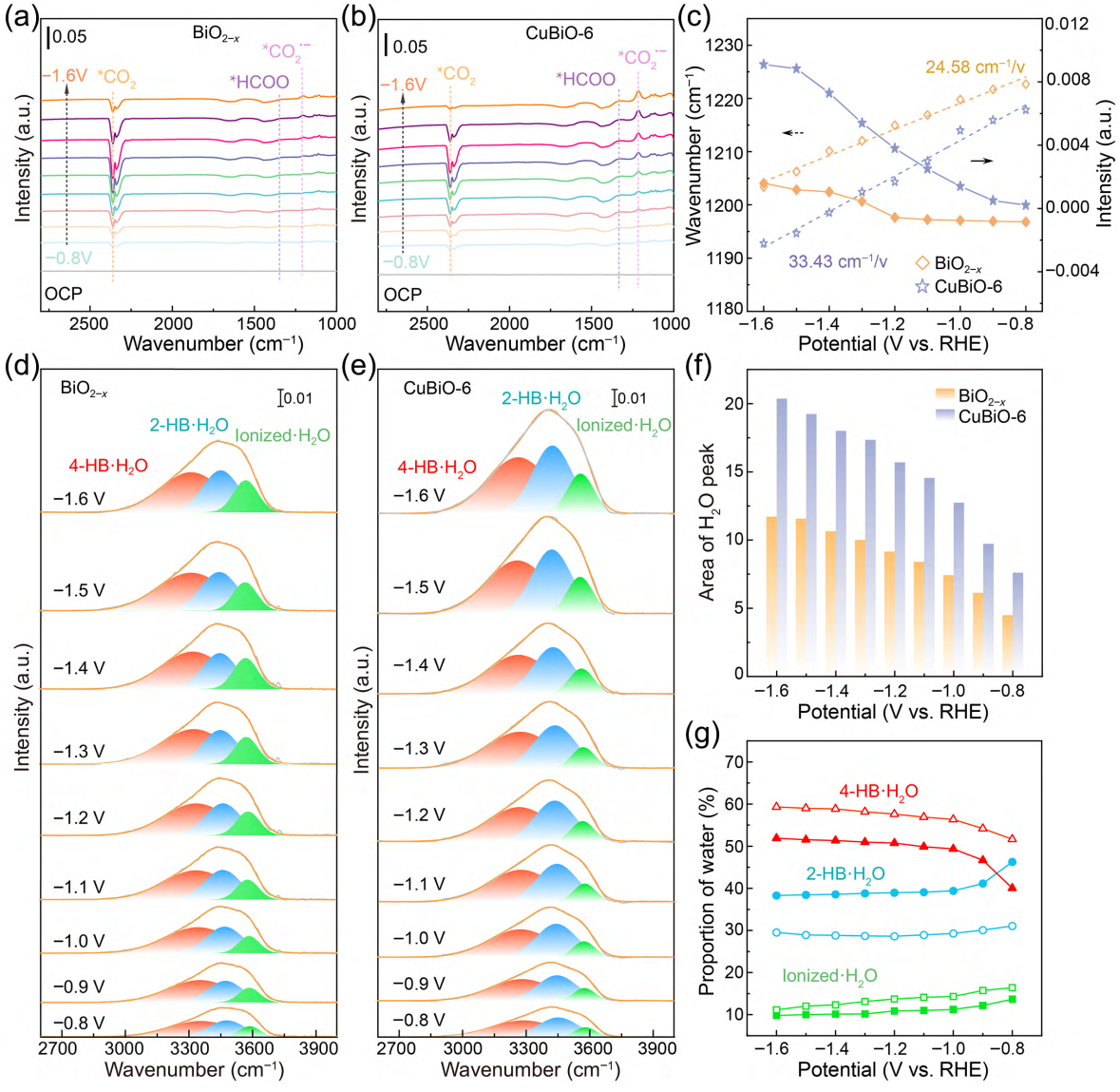

Figure 3 ((a) and (b)) *In-situ* FTIR measurements over BiO_{2-x} and CuBiO-6. (c) Changes of *COOH stretching wavenumber and the intensity of $*CO_2^{\bullet-}$ as a function of potential on BiO_{2-x} and CuBiO-6. ((d) and (e)) Gaussian fits of three O–H stretching modes from *in-situ* FTIR measurements over BiO_{2-x} and CuBiO-6. (f) Areas of the H_2O peak over BiO_{2-x} and CuBiO-6. (g) Proportion of 4-HB·H_2O, 2-HB·H_2O, and ionized H_2O over BiO_{2-x} (hollow symbols) and CuBiO-6 (solid symbols).

(ICOHP) values of −0.051 for CuBiO-6 and −0.0065 for BiO_{2-x} verify a reinforced Bi–O interaction on the doped catalyst, which facilitates CO_2 adsorption and activation. The Gibbs free energy profile of CO_2RR (Fig. 4(j)) shows that the *CO → *OCHO conversion is highly uphill on BiO_{2-x} (ΔG = 3.97 eV), whereas this step becomes much more favorable on CuBiO-6 (ΔG = 1.75 eV). Together with the *in-situ* FTIR observations, Figs. 4(k) and 4(l) outline the reaction pathway: BiO_{2-x} maintains a strong 3D HB framework dominated by 4-HB·H_2O that restricts proton transfer and severe HER, while CuBiO-6 promotes the formation of 2-HB·H_2O, generating a linear HB framework that enables faster proton transfer, boosts CO_2 hydrogenation, and improves HCOOH formation.

4 Conclusions

In conclusion, we achieved rapid proton transport within the interfacial HB network of Cu-doped BiO_{2-x} nanosheets, which substantially enhances electrocatalytic CO_2-to-HCOOH conversion. *In-situ* FTIR demonstrates that incorporation of Cu promotes H_2O dissociation to generate protons and concurrently transforms the partial of three-dimensional 4-HB·H_2O network into two-dimensional 2-HB·H_2O facilitating proton transfer. The optimized catalyst (CuBiO-6) delivers outstanding CO_2RR performance, achieving a FE of 92.4% toward HCOOH. DFT calculations indicate that this improvement performance originates from a dual mechanism: faster water dissociation and strengthened CO_2 adsorption/activation at Bi sites influenced by neighboring Cu atoms, synergistically accelerating the PCET for HCOOH formation. These findings highlight the advantage of engineering the immediate interfacial environment to realize fast proton transfer and hydrogenation for CO_2RR.

Electronic Supplementary Material: Supplementary material (SEM, TEM, XPS, LSV curves, potentiostatic curves, ultraviolet–visible (UV–vis) spectra, cyclic voltammetry (CV)

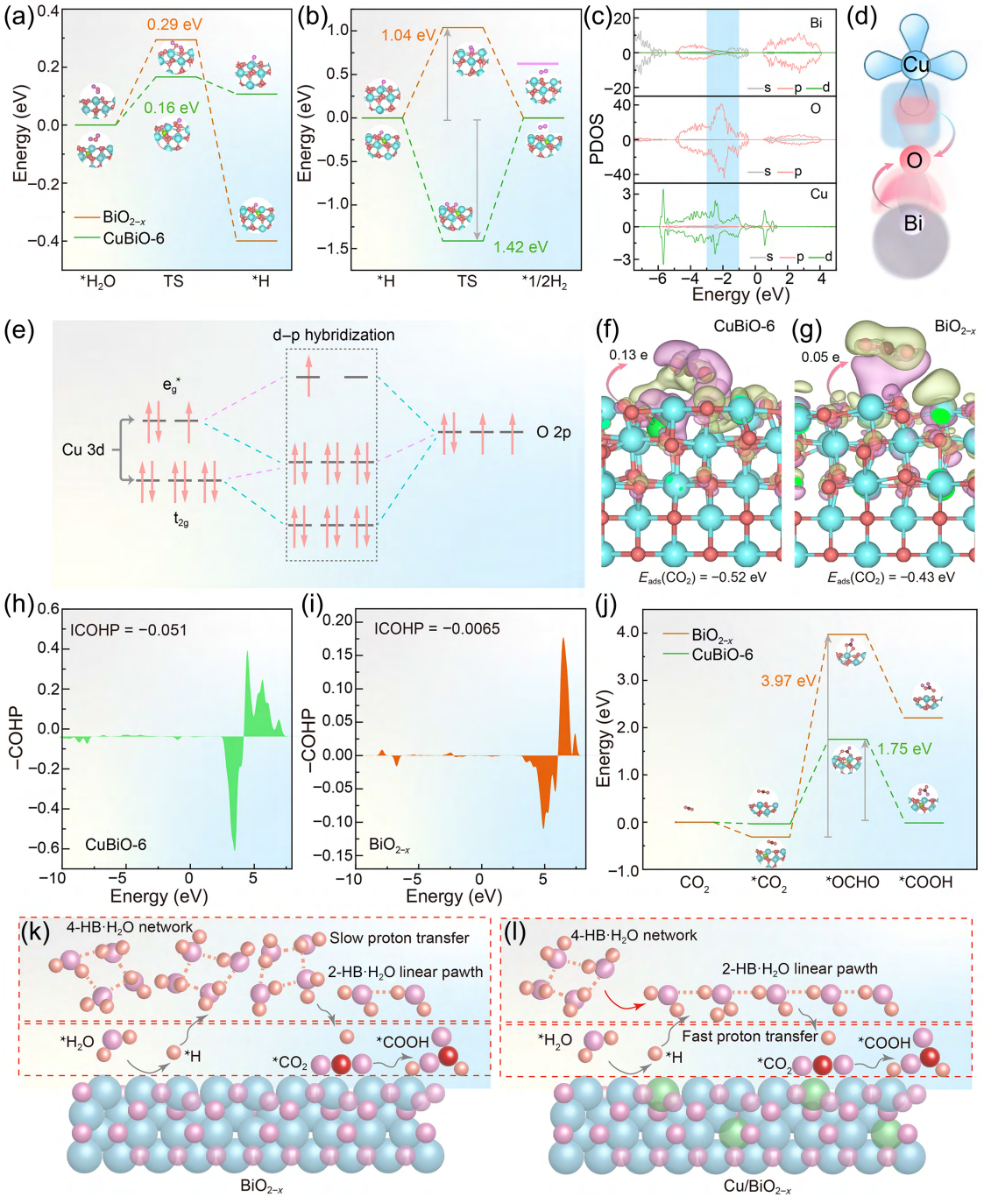

Figure 4 ((a) and (b)) The energy barrier profiles of H_2O dissociation and the dimerization of *H to H_2. (c) PDOS of CuBiO-6. (d) Schematic illustration of the electronic coupling across the CuBiO-6 structure. (e) Energy level diagram of the hybrid Cu-O molecular orbitals. ((f) and (g)) Bader charge and adsorption energy of $*CO_2$ on CuBiO-6 and BiO_{2-x}, respectively. ((h) and (i)) COHP of $*CO_2$ on CuBiO-6 and BiO_{2-x}, respectively. (j) the Gibbs free energy of CO_2RR on CuBiO-6 and BiO_{2-x}. ((k) and (l)) Schematic illustration of CO_2RR on BiO_{2-x} and CuBiO-6, respectively.

curves, *in-situ* FTIR, and DFT calculations) is available in the online version of this article at https://doi.org/10.26599/NR.2026.94908687.

Data availability

All data needed to support the conclusions in the paper are presented in the manuscript and the Electronic Supplementary Material. Additional data related to this paper may be requested from the corresponding author upon request.

Acknowledgements

This work was financially supported by the National Natural Science Foundation of China (NSFC) (Nos. 22308336 and 22508368), the City University of Hong Kong startup fund (No. 9020003), ITF-RTH-Global STEM Professorship (No. 9446006), China Postdoctoral Science Foundation (Nos. GZC20241544 and 2025M771187), and JC STEM lab of Advanced CO2 Upcycling (No. 9228005).

Declaration of competing interest

All the contributing authors report no conflict of interests in this work.

Author contribution statement

J. L.: Project administration, manuscript writing, experimental design. P. Y. L.: Material synthesis, characterization, data curation. S. X. G.: Product quantification. Z. Y. L.: Project administration, supervision. Y. Y. Z.: Funding acquisition, manuscript writing. B. L.: Funding acquisition, project administration, supervision. All the authors have approved the final manuscript.

Use of AI statement

None.

References

[1] Saha, P.; Amanullah, S.; Dey, A. Selectivity in electrochemical CO_2 reduction. *Acc. Chem. Res.* **2022**, *55*, 134–144.

[2] Ma, D. D.; Zhi, C. Q.; Zhang, Y. M.; Chen, J. T.; Zhang, Y.; Shi, J. W. A review on the influence of crystal facets on the product selectivity of CO_2RR over Cu metal catalysts. *ACS Nano* **2024**, *18*, 21714–21746.

[3] Wang, K.; Huang, K.; Wang, Z. M.; An, G. B.; Zhang, M. W.; Liu, W. H.; Fu, S.; Guo, H. Z.; Zhang, B. H.; Lian, C. et al. Functional group engineering of single-walled carbon nanotubes for anchoring copper nanoparticles toward selective CO_2 electroreduction to C_2 Products. *Small* **2025**, *21*, 2502733.

[4] Zhang, T. Y.; Han, X.; Yang, H. B.; Han, A. J.; Hu, E. Y.; Li, Y. P.; Yang, X. Q.; Wang, L.; Liu, J. F.; Liu, B. Atomically dispersed nickel(I) on an alloy-encapsulated nitrogen-doped carbon nanotube array for high-performance electrochemical CO_2 reduction reaction. *Angew. Chem., Int. Ed.* **2020**, *59*, 12055–12061.

[5] Qiao, Y.; Lai, W. C.; Huang, K.; Yu, T. T.; Wang, Q. Y.; Gao, L.; Yang, Z. L.; Ma, Z. S.; Sun, T. L.; Liu, M. et al. Engineering the local microenvironment over Bi nanosheets for highly selective electrocatalytic conversion of CO_2 to HCOOH in strong acid. *ACS Catal.* **2022**, *12*, 2357–2364.

[6] Hu, W. B.; Li, J. J.; Ma, L. S.; Su, W. Y.; Zhu, Y. P.; Li, W. H.; Chen, Y. B.; Zou, L. L.; Zou, Z. Q.; Yang, B. et al. Electrochemical reduction of CO_2 to HCOOH over copper catalysts. *ACS Appl. Mater. Interfaces* **2021**, *13*, 57462–57469.

[7] Shen, H. F.; Jin, H. Y.; Li, H. B.; Wang, H. R.; Duan, J. J.; Jiao, Y.; Qiao, S. Z. Acidic CO_2-to-HCOOH electrolysis with industrial-level current on phase engineered tin sulfide. *Nat. Commun.* **2023**, *14*, 2843.

[8] Yue, P. T.; Fu, Q.; Li, J.; Zhang, L.; Xing, L.; Kang, Z. Y.; Liao, Q.; Zhu, X. Triple-phase electrocatalysis for the enhanced CO_2 reduction to HCOOH on a hydrophobic surface. *Chem. Eng. J.* **2021**, *405*, 126975.

[9] Göttle, A. J.; Koper, M. T. M. Proton-coupled electron transfer in the electrocatalysis of CO_2 reduction: Prediction of sequential vs. concerted pathways using DFT. *Chem. Sci.* **2017**, *8*, 458–465.

[10] Zhang, Q.; Tsai, H. J.; Li, F. H.; Wei, Z. M.; He, Q. Y.; Ding, J.; Liu, Y. H.; Lin, Z. Y.; Yang, X. J.; Chen, Z. Y. et al. Boosting the proton-coupled electron transfer via Fe–P atomic pair for enhanced electrochemical CO_2 reduction. *Angew. Chem., Int. Ed.* **2023**, *62*, e202311550.

[11] Zhang, Z. Q.; Banerjee, S.; Thoi, V. S.; Shoji Hall, A. Reorganization of interfacial water by an amphiphilic cationic surfactant promotes CO_2 reduction. *J. Phys. Chem. Lett.* **2020**, *11*, 5457–5463.

[12] Liu, Z. Z.; Lv, X. M.; Kong, S. Y.; Liu, M. T.; Liu, K. H.; Zhang, J. B.; Wu, B. W.; Zhang, Q.; Tang, Y.; Qian, L. P. et al. Interfacial water tuning by intermolecular spacing for stable CO_2 electroreduction to C_{2+} products. *Angew. Chem., Int. Ed.* **2023**, *135*, e202309319.

[13] Mohandas, N.; Narayanan, T. N.; Cuesta, A. Tailoring the interfacial water structure by electrolyte engineering for selective electrocatalytic reduction of carbon dioxide. *ACS Catal.* **2023**, *13*, 8384–8393.

[14] Pang, J. Y.; Zhou, H.; Huang, Z. J.; You, X. M.; Xu, B. B.; Fu, X. B.; Weng, Y. L.; Wang, X. L.; Yao, Y. F. Interfacial water layer modulation for efficient photocatalytic CO_2 reduction. *Chem. Eng. J.* **2025**, *525*, 170446.

[15] Zheng, M.; Zhou, X.; Wang, Y. X.; Chen, G.; Li, M. X. Theoretical study on the reduction mechanism of CO_2 to HCOOH on Pd_3Au: An explicit solvent model is essential. *J. Mater. Chem. A* **2023**, *11*, 6591–6602.

[16] Dong, T.; Li, H. D.; Wang, Z. H.; Geng, Y. L.; Chang, R.; Tian, X. F.; Lai, J. P.; Feng, S. H.; Wang, L. Acidic electroreduction CO_2 to formic acid via interfacial modification of Bi nanoparticles at industrial-level current. *Nano Res.* **2024**, *17*, 5817–5825.

[17] Cai, Z.; Zhang, Y. S.; Zhao, Y. X.; Wu, Y. S.; Xu, W. W.; Wen, X. M.; Zhong, Y.; Zhang, Y.; Liu, W.; Wang, H. L. et al. Selectivity regulation of CO_2 electroreduction through contact interface engineering on superwetting Cu nanoarray electrodes. *Nano Res.* **2019**, *12*, 345–349.

[18] Tian, J. J.; Wang, M.; Shen, M.; Ma, X.; Hua, Z. L.; Zhang, L. X.; Shi, J. L. Highly efficient and selective CO_2 electro-reduction to HCOOH on Sn particle-decorated polymeric carbon nitride. *ChemSusChem* **2020**, *13*, 6442–6448.

[19] Huang, X.; Song, J. L.; Wu, H. R.; Xie, C.; Hua, M. L.; Hu, Y.; Han, B. X. Ordered-mesoporous-carbon-confined Pb/PbO composites: Superior electrocatalysts for CO_2 reduction. *ChemSusChem* **2020**, *13*, 6346–6352.

[20] Chen, W.; Chen, R. Z.; Jiang, Y. H.; Wang, Y. T.; Zhu, Y. H.; Li, Y. H.; Li, C. Z. In-induced electronic structure modulations of Bi–O active sites for selective carbon dioxide electroreduction to liquid fuel in strong acid. *Small* **2024**, *20*, 2306795.

[21] Li, W. X.; Gao, S.; Yang, C. R.; Yang, J. T.; Nisar, A.; Xiang, G. L.; Jin, J. S. Enhanced electrocatalytic CO_2 reduction to formic acid using nanocomposites of In_2O_3@C with graphene. *Nano Res.* **2024**, *17*, 5031–5039.

[22] Chen, Z.; Fan, T. T.; Zhang, Y. Q.; Xiao, J.; Gao, M. R.; Duan, N. Q.; Zhang, J. W.; Li, J. H.; Liu, Q. X.; Yi, X. D. et al. Wavy SnO_2 catalyzed simultaneous reinforcement of carbon dioxide adsorption and activation towards electrochemical conversion of CO_2 to HCOOH. *Appl. Catal. B: Environ.* **2020**, *261*, 118243.

[23] Xia, D.; Yu, H. Y.; Xie, H.; Huang, P.; Menzel, R.; Titirici, M. M.; Chai, G. L. Recent progress of Bi-based electrocatalysts for electrocatalytic CO_2 reduction. *Nanoscale* **2022**, *14*, 7957–7973.

[24] Ren, X. X.; Liu, F.; Wu, H.; Lu, Q.; Zhao, J.; Liu, Y.; Zhang, J. F.; Mao, J. J.; Wang, J.; Han, X. P. et al. Reconstructed bismuth oxide through *in situ* carbonation by carbonate-containing electrolyte for highly active electrocatalytic CO_2 reduction to formate. *Angew. Chem., Int. Ed.* **2024**, *63*, e202316640.

[25] Huang, H. L.; Wang, Y. F.; Zhang, S. J.; Huang, Y. C.; Lu, Y. R.; Chen, C. L.; Ma, J. Y.; Hu, Z. W.; Wang, J. Q.; Zhang, L. J. Role of Bi adatoms in Bi@Pd nanoparticles for electrochemical CO_2 reduction. *ACS Nano* **2025**, *19*, 15509–15521.

[26] Wang, X.; He, W. H.; Shi, J. L.; Junqueira, J. R. C.; Zhang, J.; Dieckhöfer, S.; Seisel, S.; Das, D.; Schuhmann, W. Ag-induced phase transition of Bi_2O_3 nanofibers for enhanced energy conversion efficiency towards formate in CO_2 electroreduction. *Chem.—Asian J.* **2023**, *18*, e202201165.

[27] Zhao, Y.; Liu, X. L.; Liu, Z. X.; Lin, X.; Lan, J.; Zhang, Y. L.; Lu, Y. R.; Peng, M.; Chan, T. S.; Tan, Y. W. Spontaneously Sn-Doped Bi/BiO_x core–shell nanowires toward high-performance CO_2 electroreduction to liquid fuel. *Nano Lett.* **2021**, *21*, 6907–6913.

[28] Yang, Q.; Wu, Q. L.; Liu, Y.; Luo, S. P.; Wu, X. T.; Zhao, X. X.; Zou, H. Y.; Long, B. H.; Chen, W.; Liao, Y. J. et al. Novel Bi-doped amorphous SnO_x nanoshells for efficient electrochemical CO_2

reduction into formate at low overpotentials. *Adv. Mater.* **2020**, *32*, 2002822.
[29] Wang, Y. H.; Wang, B.; Jiang, W. J.; Liu, Z. L.; Zhang, J. W.; Gao, L. Z.; Yao, W. Sub-2 nm ultra-thin $Bi_2O_2CO_3$ nanosheets with abundant Bi–O structures toward formic acid electrosynthesis over a wide potential window. *Nano Res.* **2022**, *15*, 2919–2927.
[30] Jia, L.; Sun, M. Z.; Xu, J.; Zhao, X.; Zhou, R.; Pan, B. B.; Wang, L.; Han, N.; Huang, B. L.; Li, Y. G. Phase-dependent electrocatalytic CO_2 reduction on Pd_3Bi nanocrystals. *Angew. Chem., Int. Ed.* **2021**, *60*, 21741–21745.
[31] Xue, G.; Li, Y. Q.; Du, R.; Wang, J. Y.; Hübner, R.; Gao, M.; Hu, Y. Leveraging ligand and composition effects: Morphology-tailorable Pt–Bi bimetallic aerogels for enhanced (photo-)electrocatalysis. *Small* **2023**, *19*, 2301288.
[32] Nankya, R.; Xu, Y. T.; Elgazzar, A.; Zhu, P.; Wi, T. U.; Qiu, C.; Feng, Y. G.; Che, F. L.; Wang, H. T. Cobalt-doped bismuth nanosheet catalyst for enhanced electrochemical CO_2 reduction to electrolyte-free formic acid. *Angew. Chem., Int. Ed.* **2024**, *63*, e202403671.
[33] Zhang, W. J.; Hu, Y.; Ma, L. B.; Zhu, G. Y.; Zhao, P. Y.; Xue, X. L.; Chen, R. P.; Yang, S. Y.; Ma, J.; Liu, J. et al. Liquid-phase exfoliated ultrathin Bi nanosheets: Uncovering the origins of enhanced electrocatalytic CO_2 reduction on two-dimensional metal nanostructure. *Nano Energy* **2018**, *53*, 808–816.
[34] Zhang, G. X.; Zheng, X. L.; Cui, X. M.; Wang, J.; Liu, J. H.; Chen, J. F.; Xu, Q. Doping of vanadium into bismuth oxide nanoparticles for electrocatalytic CO_2 reduction. *ACS Appl. Nano Mater.* **2022**, *5*, 15465–15472.
[35] Shen, H. D.; Zhao, Y. K.; Zhang, L.; He, Y.; Yang, S. W.; Wang, T. S.; Cao, Y. L.; Guo, Y.; Zhang, Q. Y.; Zhang, H. P. *In-situ* constructuring of copper-doped bismuth catalyst for highly efficient CO_2 electrolysis to formate in ampere-level. *Adv. Energy Mater.* **2023**, *13*, 2202818.
[36] Shen, H. D.; Zhang, J. R.; Zeng, X. L.; Yang, S. W.; Legut, D.; Wang, T. S.; Zhang, Q. Y.; Guo, S. J.; Zhang, H. P. Rational design of p-Block metal-doped bismuth via dual orbital hybridizations for ampere-level CO_2-to-formate electrosynthesis and Zn-CO_2 batteries. *ACS Catal.* **2025**, *15*, 18525–18534.
[37] Kresse, G.; Hafner, J. *Ab initio* molecular dynamics for liquid metals. *Phys. Rev. B* **1993**, *47*, 558–561.
[38] Kresse, G.; Joubert, D. From ultrasoft pseudopotentials to the projector augmented-wave method. *Phys. Rev. B* **1999**, *59*, 1758–1775.
[39] Perdew, J. P.; Burke, K.; Ernzerhof, M. Generalized gradient approximation made simple. *Phys. Rev. Lett.* **1996**, *77*, 3865–3868.
[40] Grimme, S.; Antony, J.; Ehrlich, S.; Krieg, H. A consistent and accurate *ab initio* parametrization of density functional dispersion correction (DFT-D) for the 94 elements H–Pu. *J. Chem. Phys.* **2010**, *132*, 154104.
[41] Henkelman, G.; Uberuaga, B. P.; Jónsson, H. A climbing image nudged elastic band method for finding saddle points and minimum energy paths. *J. Chem. Phys.* **2000**, *113*, 9901–9904.
[42] Maintz, S.; Deringer, V. L.; Tchougréeff, A. L.; Dronskowski, R. LOBSTER: A tool to extract chemical bonding from plane-wave based DFT. *J. Comput. Chem.* **2016**, *37*, 1030–1035.
[43] Li, J.; Wu, X. Y.; Pan, W. F.; Zhang, G. K.; Chen, H. Vacancy-rich monolayer BiO_{2-x} as a highly efficient UV, visible, and near-infrared responsive photocatalyst. *Angew. Chem., Int. Ed.* **2018**, *57*, 491–495.
[44] Li, J.; Wang, J.; Zhang, G. K.; Li, Y.; Wang, K. Enhanced molecular oxygen activation of Ni^{2+}-doped BiO_{2-x} nanosheets under UV, visible and near-infrared irradiation: Mechanism and DFT study. *Appl. Catal. B: Environ.* **2018**, *234*, 167–177.
[45] Zhang, Y. Y.; Xie, Z. K.; Ge, S. X.; Li, P. Y.; Wang, X. T.; Zhao, Z. W.; Liu, Z. Y.; Liu, B.; Li, J. *In-situ* reconstruction of Ni-modulated BiO_{2-x} for boosting electrocatalytic nitrite reduction to ammonia. *Nano Res.* **2026**, *19*, 94908176.
[46] Tan, Z. H.; Zhang, J. L.; Yang, Y. S.; Sha, Y. F.; Duan, R.; Zhong, J. J.; Han, B. X.; Hu, J. Y.; Zhao, Y. Z. BiO_{2-x} nanosheets with surface electron localizations for efficient electrocatalytic CO_2 reduction to formate. *CCS Chem.* **2023**, *5*, 133–144.
[47] Guo, W. N.; Zhang, Y. Y.; Tian, J. Q.; Liu, Z. Y.; Liu, B.; Li, J. Atomic-scale interface engineering in Bi/Bi_2O_3 heterojunctions for selective CO_2 photoreduction to methanol. *Nat. Commun.* **2026**, *17*, 983.
[48] Li, Y. X.; Zhang, Y.; Shi, L.; Liu, X. J.; Zhang, Z. B.; Xie, M. H.; Dong, Y. M.; Jiang, H. Q.; Zhu, Y. F.; Zhu, J. W. Activating inert perovskite oxides for CO_2 electroreduction via slight Cu^{2+} doping in B-sites. *Small* **2024**, *20*, 2402823.
[49] Fu, S. S.; Han, X. X.; Li, R. F.; Guo, L.; Li, Y. H.; Xu, Z. K.; Huang, X.; Chen, S. X.; Deng, S. G.; Wang, J. Regulated reconstruction of the Cu^{+}/Cu^{2+} heterointerface by cerium MOFs for the efficient CO_2 electroreduction to C_2 products. *ACS Appl. Energy Mater.* **2025**, *8*, 16498–16505.
[50] Sun, H. M.; Wen, Y. Y.; Li, Y. Q.; Fan, R.; Lu, Y. L.; Feng, C.; Liu, H.; Wang, Y. H.; Ma, Z. P.; Zhang, Y. et al. Steering the reaction pathway of CO_2 electroreduction and stabilizing Cu^{+} species by constructing the Cu^{2+}/Cu^{+} valence state fluctuation buffer zone. *Appl. Catal. B: Environ. Energy* **2026**, *381*, 125891.
[51] Chen, Y. Y.; Kang, J. H.; Zou, M. Y.; Wang, K. K.; Liu, M.; Li, W. Z. Porous carbon nanorods encapsulating bismuth nanoparticles promote p-Si nanowire array for photoelectrocatalytic CO_2 reduction to formate. *Ind. Eng. Chem. Res.* **2024**, *63*, 21831–21840.
[52] Cheng, Y. Y.; Hou, J.; Kang, P. Integrated capture and electroreduction of flue gas CO_2 to formate using amine functionalized SnO_x nanoparticles. *ACS Energy Lett.* **2021**, *6*, 3352–3358.
[53] Jia, B. Q.; Chen, Z.; Li, C. J.; Li, Z. F.; Zhou, X. X.; Wang, T.; Yang, W. X.; Sun, L. C.; Zhang, B. B. Indium cyanamide for industrial-grade CO_2 electroreduction to formic acid. *J. Am. Chem. Soc.* **2023**, *145*, 14101–14111.
[54] Scatena, L. F.; Brown, M. G.; Richmond, G. L. Water at hydrophobic surfaces: Weak hydrogen bonding and strong orientation effects. *Science* **2001**, *292*, 908–912.
[55] Zhao, R.; Wang, Q.; Yao, Y. C.; Wang, R. Z.; Zhao, L.; Hu, Z. W.; Kao, C. W.; Chan, T. S.; Li, W. H.; Zheng, Q. et al. Pd single atoms guided proton transfer along an interfacial hydrogen bond network for efficient electrochemical hydrogenation. *Sci. Adv.* **2025**, *11*, eadu1602.
[56] Ni, J. Q.; Yan, J.; Li, F. H.; Qi, H. F.; Xu, Q. Z.; Su, C. L.; Sun, L. K.; Sun, H. L.; Ding, J.; Liu, B. Atomic Co–P catalytic pair drives efficient electrochemical nitrate reduction to ammonia. *Adv. Energy Mater.* **2024**, *14*, 2400065.